Scholar Publishing Group
International Journal of Engineering Technology and Construction
https://doi.org/10.38007/IJETC.2025.060111
ISSN 2789-7176 Vol. 6, Issue 1: 109-118

Study on Bolt Stability of Corrugated Steel Webs Based on Laser Doppler Detection Method

Tianfei Qiao[1*], Nannan Peng[1], Guanhong Gong[2], Xuelin Yu[3]

China First Highway Engineering CO.,LTD.Beijing, China
Shandong Jiaotong University，Civil Engineering，Shandong, China
Beijing Municipal Construction Engineering Corporation No. 4 Co., Ltd.

[*]*corresponding author：774270320@qq.com*

Keywords: Doppler, Bolt, Finite Element

Abstract: This study investigates the stability of bolts in corrugated steel webs using a novel laser Doppler detection technique, with comparative analysis conducted on localized bolt models in ABAQUS finite element software. Fundamental frequency detection via laser Doppler reveals that the clamping force of Bolt #10 in the corrugated steel web is significantly inferior to safety levels observed in other bolts. Furthermore, finite element simulations and residual clamping force assessments were employed to model corrosion scenarios involving varying nut heights and thicknesses. An evaluation model for the clamping force loss ratio of high-strength bolts was established, demonstrating that corrosion depth profoundly impacts clamping force. Notably, trapezoidal and hourglass-shaped corrosion morphologies exhibit lower clamping force loss compared to conventional cutting. A bolt stability detection device with adjustable height and angle was designed. Combined with the positioning theory of corrugated steel web, the fundamental frequency detection found that the clamping force of bolt No. 10 was insufficient and needed on-site adjustment, providing data support for the evaluation of bolt connection reliability.

1. Introduction

The laser Doppler effect was initially discovered in acoustics. With the advent and widespread application of lasers, it gradually extended into the field of optics. Since Yeh and Cummins first observed scattered light frequency shifts in water-suspended particles in 1964—demonstrating the feasibility of laser Doppler shift technology for measuring fluid flow velocity—this technique has gained prominence due to its exceptional precision, broad measurement range, real-time capability, and non-contact nature. Concurrent with advancements in integrated optics technology, optical frequency shifting, and signal processing, laser Doppler technology achieved rapid maturation by the 1980s, finding extensive applications across medical, agricultural, and industrial domains. Driven by substantial engineering demands, its research focus expanded from fluid mechanics to solid surface analyses, such as mechanical structural flaw detection and online monitoring [1].

Presently, Germany's Polytec and Denmark's B&K lead as globally renowned manufacturers of laser Doppler vibrometers. Both companies offer integrated scanning laser Doppler vibration measurement systems, providing turnkey solutions from laser emission to data acquisition and analysis through proprietary software suites, significantly enhancing testing efficiency. Meanwhile, industry giants Analog Devices and Texas Instruments have pioneered dedicated chips achieving sampling rates up to 3 GSPS (giga-samples per second) with resolutions reaching 32 bits. Tsinghua University's Micro/Nano Electronics Center has further demonstrated breakthroughs in piezoelectric thin-film signal processing chips tailored for structural health monitoring. Leading vibrometers now typically configured with sampling rates of 10 MSPS and 24-bit resolution, whereas high-end models support up to 1 GSPS/28-bit configurations [2].

In the late 1970s, Stanbridge and Ewins pioneered the continuous-scan laser Doppler vibrometry (CSLDV) method. Initially aiming to characterize disk vibration modes, they attached a microphone to the edge of a vibrating disk performing circumferential scans. Analysis revealed that the acquired signals were modulated by both the scanning path and structural mode shapes, ultimately enabling successful modal reconstruction through demodulation techniques. In 1999, the researchers expanded this methodology to laser Doppler vibrometry, achieving diverse scanning patterns including sinusoidal-velocity linear paths, constant-velocity linear trajectories, and spiral sweeps—catalyzing extensive global research on CSLDV technology.

Concerning three-dimensional structures, Schwingshackl et al. developed an internal measurement approach for cylindrical vessels. They engineered a rotational test platform to scan internal surfaces of drum-type structures, subsequently implementing the method for casing diagnostics in operational aeroengines. Concurrently, Stanbridge and Ind et al. devised an external laser-scanning strategy for cylindrical configurations. By mounting test specimens on rotary stages, they attained substantially denser spatial resolution of operational deflection shapes compared to conventional methods.

2. Principle of Laser Doppler Technology

Laser Doppler Velocimetry (LDV) is a non-contact, high-precision velocity measurement technique leveraging optical interference and the Doppler effect. By detecting frequency shifts in scattered light from moving objects, LDV achieves high-accuracy vectorial velocity measurement. Compared to traditional contact methods like piezoelectric sensors, LDV offers distinct advantages: non-invasiveness, superior spatiotemporal resolution, and directional sensitivity. These capabilities render it indispensable for complex flow analysis, mechanical vibration monitoring, and biomechanical dynamics research.

The interaction between emitted laser and particles is a crucial link in laser Doppler technology. In this process, specific laser equipment is needed to generate appropriate laser. We usually use lasers such as Him - Ne lasers, Ar ion lasers, or new - generation solid - state lasers. Each of these lasers has its own characteristics: He - Ne lasers output laser with stable wavelength and good coherence; Ar ion lasers can generate high - power laser; and new - generation solid - state lasers have advantages in terms of volume, efficiency, etc. Their common function is to generate high - power laser with specific wavelength, which is the basis for a series of subsequent operations.

The generated laser needs to go through a series of transmission steps. First, it passes through an optical splitter, which can split the laser as required, enabling the laser to better adapt to subsequent transmission and use. Then, the laser travels through a single-mode polarization-maintaining optical fiber, which can ensure the stability of the laser's polarization state during transmission and reduce signal loss. It then passes through an optical fiber coupler to efficiently couple the laser into the laser emission probe.

The laser emission probe emits the laser and focuses it at the beam waist. The beam waist is the smallest area formed after the laser is focused, where the smallest measurement volume is created. When measuring fluid velocity, since the fluid itself may be difficult to directly produce obvious scattering effects on the laser, it is necessary to add tracer particles to the fluid. These tracer particles move along with the fluid. When the laser irradiates them, scattering occurs, and the scattered light carries the movement information of the particles. By analyzing this information, the velocity of the fluid can be obtained.

3. Generation of Doppler frequency shift

The generation of Doppler frequency shift is due to the relative motion between the tracer particles (which move with the fluid) and the laser source. According to the optical Doppler effect, the frequency of the laser reflected from the tracer particles will shift, that is, a Doppler frequency shift is generated. The magnitude of this frequency shift has a linear relationship with the moving speed of the tracer particles (i.e., the fluid) and is not affected by temperature and pressure.

The generation mechanism of Doppler frequency shift is a core physical phenomenon in the interaction between light and moving matter, whose essence can be interpreted from both the classical wave theory and the framework of relativity. When a monochromatic laser beam irradiates tracer particles moving with the fluid, the particles act as secondary light sources, and the frequency of their scattered light shifts relative to that of the incident light.

The relationship between this frequency shift and the particle motion velocity follows the formula:

$$\Delta f = v \cdot \cos\theta \cdot \frac{f_0}{c}$$

In the formula, θ is the angle between the particle motion direction and the laser beam.c is the speed of light.

From the analysis of classical wave theory, a moving particle is equivalent to a moving wave source, and the spherical wavefront it emits will be compressed or stretched due to the motion. When the particle moves towards the light source, the number of wave crests passing through the observation point per unit time increases, resulting in an increase in frequency (blue shift); conversely, the frequency decreases (red shift). This linear relationship between the frequency shift and velocity holds under non-relativistic conditions. Experimental verification shows that in the velocity range of 0-1000m/s, the linearity deviation is less than 0.05%.

From the perspective of quantum mechanics, the collision between a photon and a moving particle can be regarded as an inelastic scattering process. The incident photon carries momentum h/λ_0 , The change in the momentum of the particle after the collision Δp result in a change in the momentum of photons， which in turn causes a frequency shift.

In actual measurements, frequency shift signals are affected by various factors: ① Changes in the incident angle cause the frequency shift to exhibit cosine modulation, which requires the elimination of angle sensitivity through a dual-beam orthogonal configuration; ② Changes in fluid temperature affect particle Brownian motion, but the frequency shift only reflects the macroscopic flow velocity. Experiments show that within the range of -40℃ to 150℃, the frequency shift error caused by temperature is less than 0.1%; ③ The refractive index change caused by pressure changes can be compensated by wavelength locking technology, and within the pressure range of 10MPa, the measurement deviation is controlled within 0.3%. To ensure measurement accuracy, a standard calibration system needs to be established. Common methods include the rotating disk

method (verifying linearity in the range of 0-50m/s), the laminar flow pipe method (verifying accuracy of ±0.5%), and the PIV comparison method (verifying dynamic response consistency).

This technology has extensive application value in the engineering field. In the biomedical field, by measuring the frequency shift of scattered light from red blood cells, blood flow velocity can be accurately calculated (with a precision of ±0.01mm/s); in the aerospace field, it can be used for high-speed flow field analysis in scramjet combustors (Mach number 6); in the field of materials science, it can track the movement trajectory of nanoparticles. The latest research combines chirped laser technology to expand the measurable speed range to 10^4m/s, breaking through the application limit of the traditional Doppler effect and providing a new means for high-speed impact flow field research. Its non-contact, high-precision, and wide-range characteristics make it an indispensable part of modern measurement technology.

4. Project Overview

K26+203.8 Tuhai River Grand Bridge, with the starting pile number K25+670.3 and the ending pile number K26+737.3, has a total length of 1067.0m. The span composition of the bridge is 13×30 + 75 + 130 + 75 + 13×30m, and the net width of the bridge deck is 11.75m. Type 80 modular expansion joints are installed at abutments 0 and 29, and piers 3, 6, 9, 20, 23 and 26; Type 240 modular expansion joints are installed at piers 13 and 16; and the rest parts are of continuous bridge deck. For the superstructure, the main bridge adopts a corrugated steel web cantilever cast continuous beam, and the approach bridge uses prestressed concrete (post-tensioned) simply supported T-beams with continuous bridge deck. For the substructure, the abutments are ribbed slab abutments with pile foundations; the main bridge piers and transition piers are all wall-type piers with group pile foundations; and the approach bridge adopts column-type piers with pile foundations.

The axis is determined by setting out control point 1 with a total station, that is, determining the lateral spatial position of the steel web on the bridge. Then, the elevation of the top center of the steel web at the end of the segment is obtained through theoretical calculation. After that, the steel web is pulled to the specified position for fixing. Finally, the Bn point of the steel web is re-measured with a total station, and the error is confirmed by comparing with the theoretical calculation.

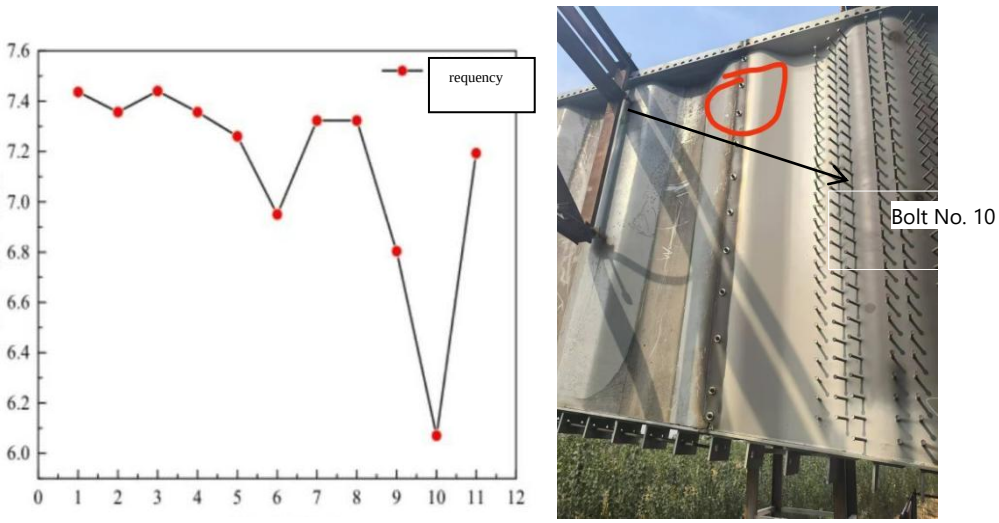

Fig.1 Bolt Test Results and On-Site Situation

After repeated on-site measurements and comprehensive data extraction, the laser Doppler

fundamental frequency detection results show that the clamping force of bolt No.10 on the corrugated steel web is obviously insufficient, which is significantly lower than the safety level of other bolts,as shown in Figure1. It is suggested to adjust the bolt clamping force on site to prevent potential impacts on the corrugated steel web caused by insufficient clamping of the bolt.

5. Finite Element Simulation Verification of High-Strength Bolted Joint Test Pieces After Laser Doppler Scanning

During the corrosion process along the height of the high-strength nut, the strain distribution diagram of the high-strength bolt with a 200kN clamping force applied to the M22 high-strength bolt is shown in Figure 2. It can be seen from Figure 2 (a) that when the high-strength bolt is not subject to cross-sectional damage, the stress generated by the nut gradually decreases from top to bottom.

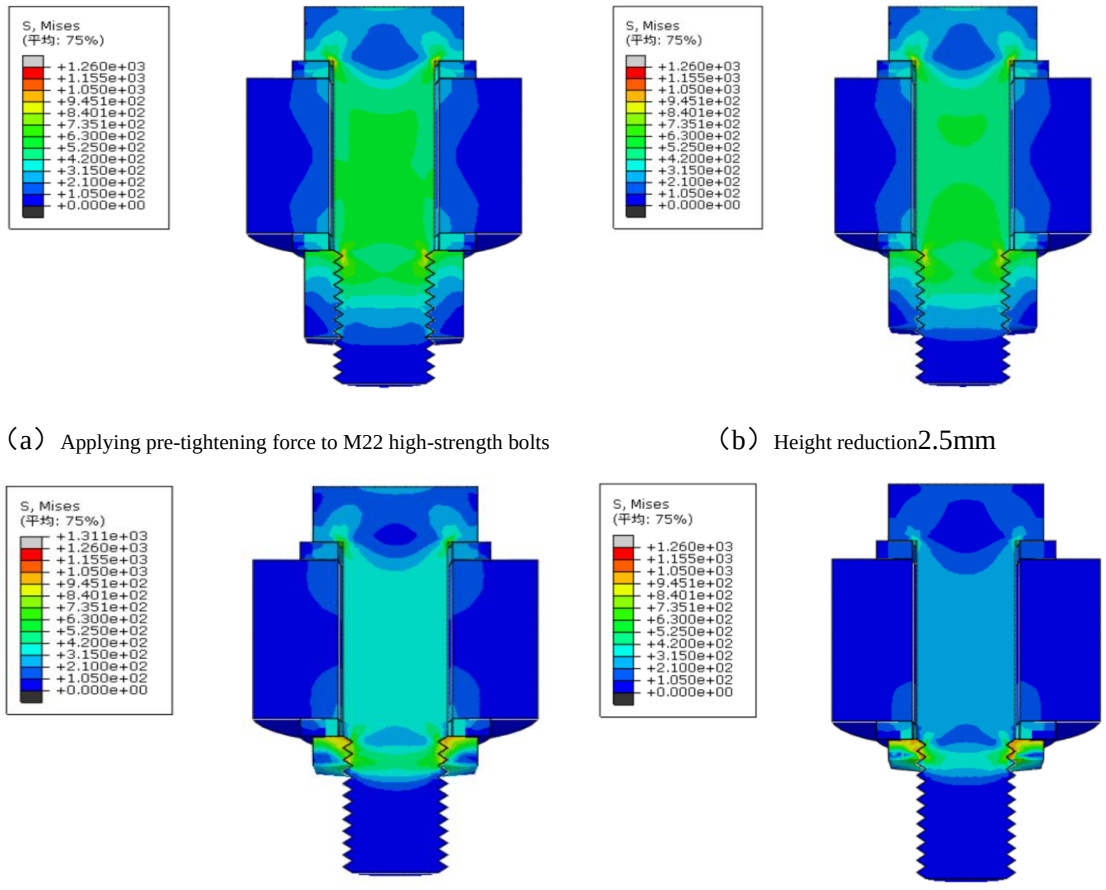

（a） Applying pre-tightening force to M22 high-strength bolts

（b） Height reduction2.5mm

（c） Height reduction15mm

（d） Height reduction17.5mm

Fig. 2 Stress distribution diagram of M22 high-strength bolts during the corrosion process of nuts along their height

The axial stress distribution curves of M22 high-strength bolts along the height-thinning path L1 are shown in the figures respectively. It can be seen that the strain is evenly distributed in the middle section, that is, the strain is evenly distributed in the bolt shank part. When the height is thinned to 10 mm, the stress variation of the bolt shank increases, and in the subsequent process of thinning the nut height, the strain variation shows an increasing trend all the time,as shown in Figure 2.

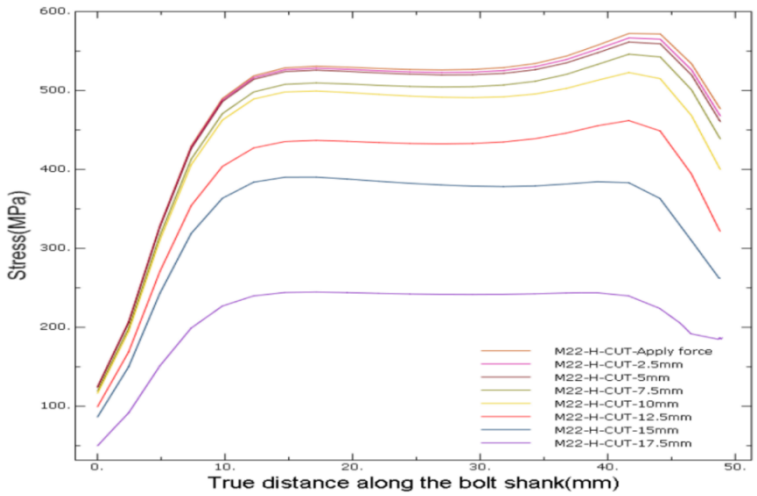

Fig. 3 Axial stress distribution of M22 high-strength bolts with the nut thickness reduced along its height

When the height of the high-strength nut is thinned by 2.5mm, 5mm, 7.5mm, 10mm, 12.5mm, 15mm and 17.5mm respectively, the axial strain decreases by 2.0%, 3.9%, 6.7%, 9.2%, 19.9%, 30.1% and 55.4% respectively compared with the initial state of the high-strength bolt, as shown in Table1.

Table 1 Axial Strain of M22 High-Strength Bolt Shank When the Thickness of the Nut Is Reduced Along Its Height

reduction amount/mm	Path L1	loss ratio/%
Initial	541.391	0
2.5	530.314	-2.0
5	520.515	-3.9
7.5	505.004	-6.7
10	491.438	-9.2
12.5	433.911	-19.9
15	378.375	-30.1
17.5	241.639	-55.4

The stress distribution diagram of the M20 high-strength bolt under a clamping force of 200 kN is shown in Figure 3The results displayed in the stress distribution diagram are essentially the same as those of the M22 high-strength bolt.

The axial stress distribution curves of the M20 high-strength bolt along the thinning path L1 in the height direction are as shown in the figure 4. The strain variation trend is essentially consistent with that of the M22 high-strength bolt.

When the height of the high-strength nut is reduced by 2mm, 4mm, 6mm, 8mm, 11mm, 14mm and 17mm respectively, the axial strain is reduced by 1.4%, 2.4%, 3.7%, 7.5%, 17.2%, 40.2% and 72.1% respectively compared with the initial state of the high-strength bolt, as shown in the table.

Through the comparison between M20 and M22 high-strength bolts, it can be confirmed that under the condition of the same corrosion depth along the height of the nut, the clamping force loss ratio of M20 high-strength bolts is greater than that of M22 high-strength bolts, indicating that the corrosion along the height of the nut has a significant impact on the clamping force. When the thinning amount of the high-strength bolt along the height of the nut is less than 4mm and 6mm, it has no obvious effect on the clamping force of M20 and M22 high-strength bolts respectively.

However, when the thinning amount of the nut exceeds 4mm and 6mm, not only does the axial strain of the bolt shank decrease significantly, but also the remaining part of the nut undergoes obvious deformation, seriously affecting the bearing capacity of the high-strength bolt joint. According to the strain distribution diagram of the high-strength bolt thinned along the height of the nut:

(1) The strain in the middle of the bolt shank of the high-strength bolt is proportional to the remaining height of the high-strength nut after corrosion.

(2) Stress is concentrated at the junction of the bolt head and the nut and washer.

(3) As the height of the nut decreases, after amplifying the deformation scaling factor, it can be seen that the center of the nut gradually shows a trend of disc-shaped deformation, and its edge shows a warping trend.

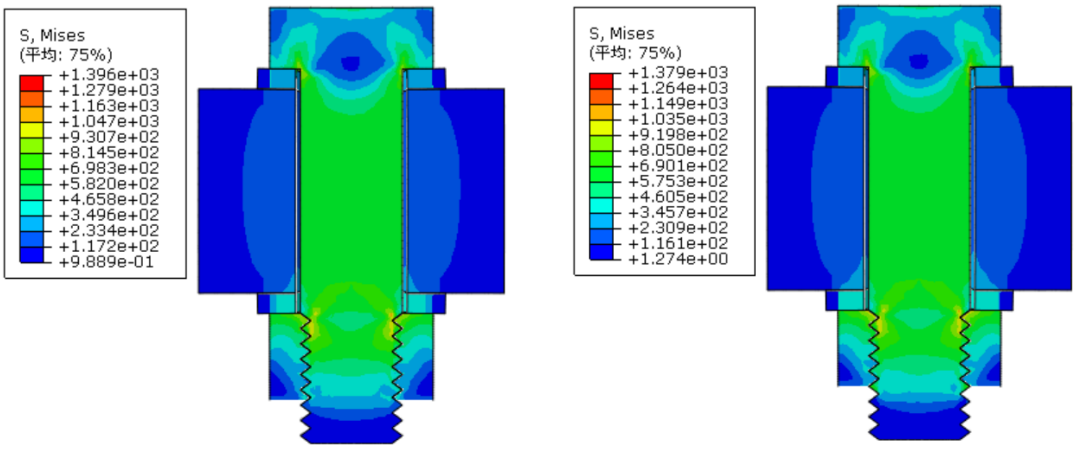

（a）Height reduction4mm　　（b）Height reduction6mm

Figure 4 Stress Distribution Diagram of M20 High-Strength Bolts During the Corrosion Process of Nuts Along Their Height

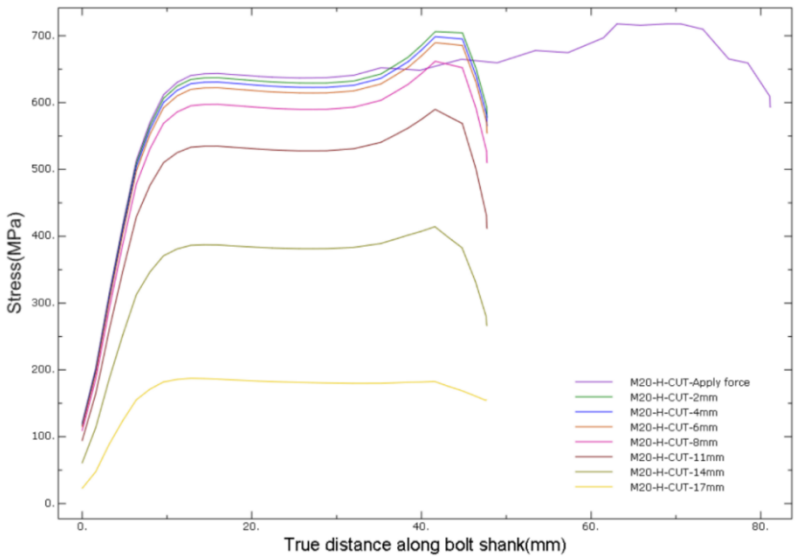

Figure 5 Axial Stress Distribution of M22 High-Strength Bolts with Nut Thickness Reduced Along Its Height

6. Finite Element Simulation of Corrosion along the Thickness of Nuts

During the corrosion process along the thickness of the high-strength nut, due to different cutting methods, the interaction of the birth-death elements of the finite element model and the meshing of the high-strength bolt are shown in Figure 5.

The strain distribution diagram of the M22 high-strength bolt finite element model after applying a clamping force of 200 kN is shown in the figure 5.

When the thickness of the high-strength nut is reduced by 1.5 mm, 3 mm, and 4.5 mm respectively, the stress loss ratios of the axial stress to the initial stress of the high-strength bolt are shown in Table 2.

Table 2 Axial Stress of M22 High-Strength Bolt Shank When the Thickness of the Nut Is Reduced Along Its Thickness

thinning amount/mm	Path L1	loss ratio/%
Initial	528.445	0
1.5	496.561	-6.0
3	388.586	-26.5
4.5	264.459	-50.0

The strain distribution diagram of the M20 high-strength bolt finite element model after applying a clamping force of 200 kN.

The curve diagram of axial stress distribution along path L1 for M20 high-strength bolts with thickness reduction is shown in the figure 5.

When the thickness of the high-strength nut is reduced by 2.0 mm, 3.5 mm, and 5.0 mm respectively, the stress loss ratios of the axial stress to the initial stress of the high-strength bolt are shown in Table 2.

The strain distribution diagram of the M16 high-strength bolt finite element model after applying a clamping force of 150 kN is shown in Figure 6.

The curve diagram of axial stress distribution along path L1 for M16 high-strength bolts with thickness reduction is shown in Figure 7.

When the thickness of the high-strength nut is reduced by 1.5mm, 2.5mm, and 4.0mm respectively, the stress loss ratios of the axial stress to the initial state of the high-strength bolt are shown in the following table.

A comparison of M16, M20 and M22 high-strength bolts confirms that under the condition of the same corrosion depth along the nut thickness, the clamping force loss ratio of M22 high-strength bolts is the smallest, and the corrosion along the nut thickness has a significant impact on the clamping force. It can be seen from the strain distribution diagram of high-strength bolts with the nut thickness thinned:

(1) The stress in the middle of the shank of the high-strength bolt decreases as the thickness of the high-strength nut is thinned.

(2) The strain is concentrated at the bolt head and the junction between the remaining part of the nut (after thickness reduction) and the washer.

7. Finite Element Simulation of Corrosion along the Three-Side Thickness of the Nut

During the corrosion process along the three-side thickness of the high-strength nut, due to different cutting methods, the interaction of the birth-death elements of the finite element model and the mesh division of the high-strength bolt are shown in the figures.

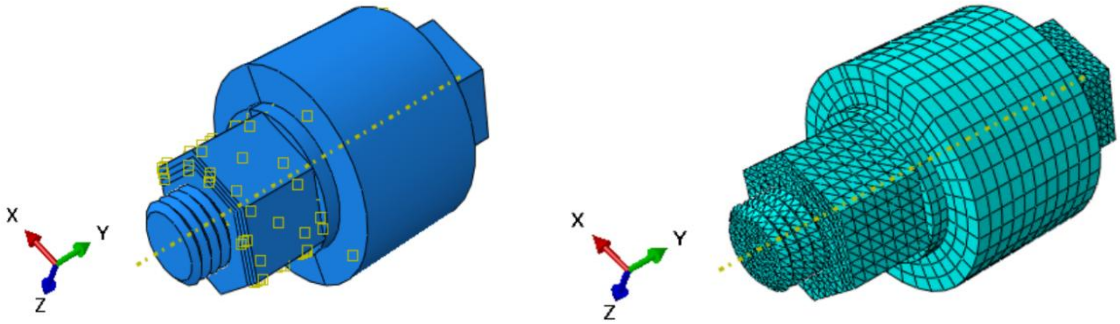

（a） Interaction between birth-death modules

（b） Mesh generation of the model for cutting along the nut thickness

Figure 6 Finite Element Model of Cutting Along the Thickness of Three Sides of the Nut

The strain distribution diagram of the M22 high-strength bolt finite element model after applying a clamping force of 220 kN is shown in the figure.

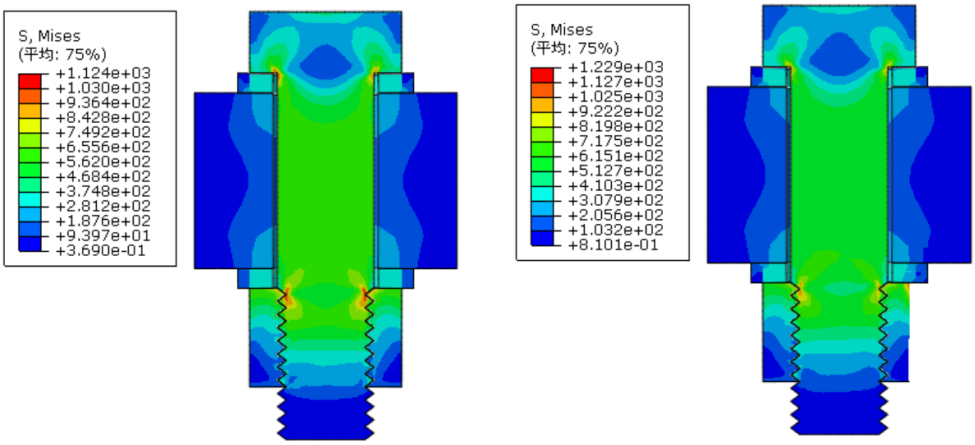

（a）Applying pre-tightening force to M22 high-strength bolts（b）A full circle of thickness reduction1.5mm

Figure 7 Stress Distribution Diagram of M22 High-Strength Bolts During the Corrosion Process of Nuts Along the Thickness of Their Three Sides

The curve diagram of axial stress distribution along path L1 where the thickness of M22 high-strength bolt is reduced on three sides is shown in the figure.

When the thickness of the high-strength nut is reduced by 1.5 mm, 3.0 mm, and 4.5 mm respectively, the stress loss ratios of the axial stress to the initial stress of the high-strength bolt are shown in the table.

According to the stress distribution diagram of high-strength bolts with the thickness of three sides of the nut thinned, it can be seen that:

(1) The strain in the middle of the shank of the high-strength bolt decreases as the thickness of the three sides of the high-strength nut is thinned.

(2) With each thinning of the thickness along the three sides of the nut, the strain generated by the nut at the bolt shank shifts to the thinned cutting surface of the nut, and the stress at the thinned side of the bolt shank is less than that at the non-thinned side.

(3) It can be seen from the comparison that under the condition that the average corrosion depth from the cutting to the cutting edge along the nut thickness is the same for high-strength bolts of the

same specification, the influence of cross-sectional damage on the loss ratio of the clamping force of the bolt shank in the way of cutting along the three-side thickness of the nut is less than that in the way of cutting along the nut thickness.

8. Conclusions

(1) The FARO scanner was used to perform 3D laser scanning on the construction hanging basket and corrugated steel web. Through point cloud data processing and reverse modeling, the high-precision restoration of the 3D shape of the components was realized. The deviation between the actual measurement and the design drawings was controlled within 1%, which verified the accuracy and efficiency of this technology in bridge construction monitoring and proved the application prospect of 3D laser scanning in engineering.

(2) A bolt stability detection device with adjustable height and angle was designed. Combined with the positioning theory of corrugated steel web, the fundamental frequency detection found that the clamping force of bolt No. 10 was insufficient and needed on-site adjustment, providing data support for the evaluation of bolt connection reliability.

(3) Finite element simulation and residual clamping force evaluation were used to simulate corrosion scenarios with different nut heights and thicknesses, and an evaluation model for the clamping force loss ratio of high-strength bolts was established (such as the loss ratio equation for M22.

References

[1] Wang Chao. Experimental study on shear performance of composite girder bridge with variable cross-section corrugated steel webs. Nanjing: Southeast University, 2016.

[2]Li Yunsheng, Li Mengbiao, Wang Yaping, et al. Study on bending-torsion performance of steel-concrete composite beams with corrugated steel webs [J]. Journal of Hebei University of Science and Technology, 2022, 43 (1): 99-109.